Localized thinning for strain concentration in suspended germanium membranes and optical method for precise thickness measurement

Cite as: AIP Advances **8**, 115131 (2018); https://doi.org/10.1063/1.5050674
Submitted: 02 August 2018 . Accepted: 15 November 2018 . Published Online: 28 November 2018

P. O. Vaccaro, M. I. Alonso, M. Garriga, J. Gutiérrez, D. Peró, M. R. Wagner, J. S. Reparaz, C. M. Sotomayor Torres, X. Vidal, E. A. Carter, P. A. Lay, M. Yoshimoto, and A. R. Goñi

Localized thinning for strain concentration in suspended germanium membranes and optical method for precise thickness measurement

P. O. Vaccaro,[1,2,a] M. I. Alonso,[2] M. Garriga,[2] J. Gutiérrez,[2,3] D. Peró,[2] M. R. Wagner,[4,5] J. S. Reparaz,[4] C. M. Sotomayor Torres,[1,4] X. Vidal,[3] E. A. Carter,[6] P. A. Lay,[6] M. Yoshimoto,[7] and A. R. Goñi[1,2]
[1]*ICREA, Passeig Lluís Companys 23, E-08010 Barcelona, Spain*
[2]*Institut de Ciència de Materials de Barcelona (ICMAB-CSIC), Esfera UAB, E-08193 Bellaterra, Spain*
[3]*Department of Physics and Astronomy, Macquarie University, 2109 NSW, Australia*
[4]*Catalan Institute of Nanoscience and Nanotechnology (ICN2), Campus de la UAB, E-08193 Bellaterra, Spain*
[5]*Institut für Festkörperphysik, Technische Universität Berlin, Hardenbergstr. 36, 10623 Berlin, Germany*
[6]*School of Chemistry and Sydney Analytical, University Sydney, Sydney, NSW 2006, Australia*
[7]*Department of Electronics, Kyoto Institute of Technology, Sakyo, Kyoto 606-8585, Japan*

(Received 2 August 2018; accepted 15 November 2018; published online 28 November 2018)

We deposited Ge layers on (001) Si substrates by molecular beam epitaxy and used them to fabricate suspended membranes with high uniaxial tensile strain. We demonstrate a CMOS-compatible fabrication strategy to increase strain concentration and to eliminate the Ge buffer layer near the Ge/Si hetero-interface deposited at low temperature. This is achieved by a two-steps patterning and selective etching process. First, a bridge and neck shape is patterned in the Ge membrane, then the neck is thinned from both top and bottom sides. Uniaxial tensile strain values higher than 3% were measured by Raman scattering in a Ge membrane of 76 nm thickness. For the challenging thickness measurement on micrometer-size membranes suspended far away from the substrate a characterization method based on pump-and-probe reflectivity measurements was applied, using an asynchronous optical sampling technique. https://doi.org/10.1063/1.5050674

INTRODUCTION

Electrical and optical properties of semiconductor materials can be tailored by applying strain.[1] Strained materials have found application in devices such as semiconductor lasers,[2] transistors,[3] optical modulators,[4] and photodetectors,[5] among others. In particular, tensile stress applied to Ge has the potential to improve light emission by modifying the electronic band structure, transforming this indirect band gap material into a direct gap semiconductor.[6,7] This transition is predicted to occur at around 2% biaxial strain parallel to the (100) crystallographic plane[8–10] and above 4% uniaxial tensile strain along the [100] crystallographic direction.[11] Uniaxial strain exceeding the threshold for obtaining the direct band gap has been demonstrated[12,13] but its implementation in optoelectronic devices is technologically challenging. In this respect, Ge has also the important advantage of being suitable for monolithic integration on Si substrates and, eventually, allowing integration of laser diodes in CMOS technology.

[a]Electronic mail: pablo.vaccaro@icrea.cat

Biaxial tensile strain can be introduced in Ge epitaxial layers deposited on Si substrates due the difference in thermal expansion coefficient between the two materials. This coefficient is larger in Ge than in Si. Ge layers annealed at a high temperature will develop tensile strain when cooled down to room temperature because Ge tends to contract more than Si.[14] Unfortunately, the large lattice parameter difference of ca. 4% between Ge and Si leads to formation of a network of misfit dislocations near the interface between both materials and threading dislocations through the Ge layer. These dislocations (and microstructural defects in general) degrade the optical and electronic properties of the Ge layer by reducing minority carrier lifetime and quantum efficiency of light emission.[15,16] Dislocations are therefore undesirable, particularly in thin Ge layers.

Judicious patterning of the Ge layer and its partial release from the substrate by the selective etching of Si allows for a redistribution of strain in the suspended membrane, such that a high tensile strain can be concentrated in a desired region of the structure. The initially low biaxial strain is then concentrated, for example, in a narrow neck in the center of a bridge, where it becomes uniaxial. Here, we established a fabrication process of Ge membranes with uniaxial tensile strain, where not only width but also thickness of the neck connecting the bridge is controlled for strain concentration. Besides, the highly defective Ge near the interface to Si is eliminated and only the higher quality Ge far from the interfaces is kept in the membrane. Of great value, our fabrication methods are suitable for large scale production and compatible with CMOS technology. We have used scanning and transmission electron microscopy (SEM and TEM, respectively) to evaluate the number of microstructural defects in the Ge layers. The thickness of the as-grown layers has been measured by ellipsometry, whereas that of the suspended membranes has been determined by pump-and-probe reflectivity measurements based on an asynchronous optical sampling technique (ASOPS).[17] We have locally characterized the tensile strain of the Ge membranes using micro-Raman spectroscopy.[18] Comparison of Raman measurements and results from simulations using finite element methods (FEM) gave further insight into the strain distribution in the membranes and enabled adjusting tensile strain by proper design of the structure and its geometry. Our goal is to study the effects of uniaxial strain in Ge membranes with thicknesses in the range of tens of nanometers.

METHODS

Si and Ge layers were deposited on double-side polished, high-resistance Si wafers by molecular beam epitaxy. The deposition sequence of the layers is shown in Fig. 1. After oxide desorption at 850 °C, a Si layer was grown at 660 °C to obtain an ideal Si surface. Then temperature was decreased to 400 °C and a 30 nm layer of Si was deposited. This low temperature Si (LT-Si) layer has a compliant effect that helps to relax the strain in the subsequently deposited Ge.[19] The temperature was further reduced to 200 °C and a 10 nm layer of Ge was grown. The low temperature prevented Ge atoms from moving on the surface, hindering the Stranski-Krastanow growth mode and kept a flat growth front. While growing the next 20 nm of Ge, the substrate temperature was increased slowly until it reached 400 °C. This growth sequence produced a network of misfit dislocations that prevented build-up of compressive strain in the Ge layer due to the smaller lattice parameter of Si. The dislocations appear mostly within the two low temperature Si and Ge thin sections. In particular, a high density of point defects in the Ge grown at low temperature contributes to effectively relax the mismatch strain and to act as getter sites that reduce the threading dislocation density.[20] The next step consisted of deposition of a 400-nm thick layer of Ge at 500 °C. This layer had little residual compressive strain. Finally, a Si cap layer was deposited on top to protect the Ge surface. This structure was subsequently annealed at 700 °C for 30 min in the same growth chamber. This annealing temperature is sufficient to reduce further the threading dislocation density[21] to our measured value of $1x10^7$ cm^{-2}. At the same time, since Ge has a thermal expansion coefficient more than two times larger than Si, a compressive strain develops in the Ge layer when temperature is raised up to 700 °C. The high temperature annealing allows gliding of the remaining threading dislocations and the 400 nm thick Ge layer becomes nearly strain free again while kept at high temperature. Finally, during a fast cooling process of the wafer down to room temperature, the Si wafer contracts less than the Ge layer, resulting in a final *tensile biaxial strain* in the Ge. The highest biaxial tensile strain attainable by this growth procedure is in the range of 0.1 – 0.2%.

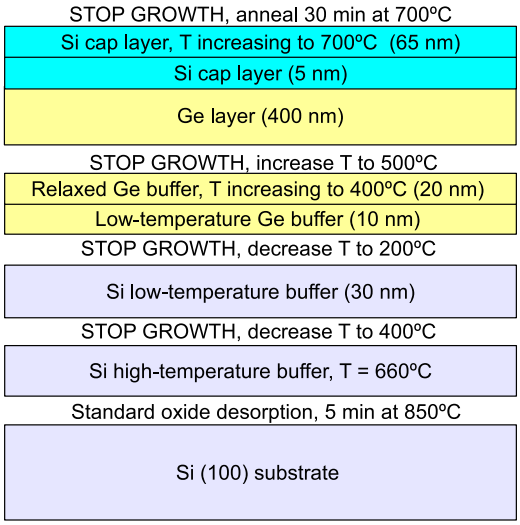

FIG. 1. Sketch of the epitaxial structure and growth process of tensile-strained Ge layers.

To produce the tensile strained Ge membranes, we have established a fabrication process with two steps of selective etching of Si through which we also tailor the Ge layer thickness. Figures 2(a)–2(d) show schematically the fabrication process. (a) A pattern of bridges with a narrow neck in the center, oriented along (100) direction, was defined by means of optical lithography and etched through the Ge layer and a few hundred nanometers depth in the Si substrate using reactive ion etching with CF_4 gas. (b) The Si cap layer and the Si below the neck were selectively removed using a hot KOH water solution (40 wt% at 85 °C). (c) Next, the Ge layer was thinned by etching in water-diluted H_2O_2 (1:100). In this step, the Ge layer was etched from the top uniformly on all exposed surfaces, and from the underside only in the (exposed) neck region. This etching step eliminated the Ge layer close to the Si/Ge interface, where most of the misfit dislocations are located. Besides, any SiGe alloy formed during the post-growth anneal at the Si/Ge interfaces is etched away at this step. Therefore, the Ge membrane in the neck region was thinner and had a substantially lower density of defects than that in the broader bridge area. (d) A longer etching in hot KOH solution finally released the bridges from the substrate. At this stage, tensile strain in the bridges decreased slightly by straining the much thinner and narrower necks. Figure 2(e) shows an optical microscope picture of bridge and neck. The neck and thinner edges of the bridge have a lighter color than the central region of the bridges due to the difference in thickness. Figure 3 shows a cross-section SEM micrograph of a broken bridge. Difference in thickness between the central region and the periphery of the bridge is clearly observed (the neck has the same thickness as the periphery of the bridge). However, our SEM resolution and angle of observation do not allow us to obtain an accurate value of the Ge membrane thickness.

Strain status of the suspended bridge-neck-bridge structures was accurately determined from the frequency of the longitudinal optical (LO) phonon mode of Ge measured by Raman scattering. Raman spectra were collected at room temperature in backscattering geometry with a high-resolution LabRam HR800 spectrometer using a grating with 1800 lines per millimeter and equipped with a liquid-nitrogen cooled charge coupled device (CCD) detector. For excitation we used the 632.8 nm line from a He–Ne gas laser. The laser beam was focused onto the sample using a long working distance microscope objective with 100× magnification, yielding a spot with a diameter of 1.5 μm. The measured power density at the sample position was 80 W/cm^2, corresponding to the maximum incident laser power that could be safely used before a redshift of the Raman peak in the neck region was observable. Such a shift as a function of laser power was ascribed to laser heating, a recurrent problem when dealing with very thin suspended membranes with fairly low thermal conductance, as was the case here. This ensured that any observed shift of the LO Raman mode of Ge was caused by the built-in strain and not to spurious temperature effects induced by the laser. Mapping of strain by Raman spectroscopy was performed with a Renishaw inVia Reflex confocal Raman

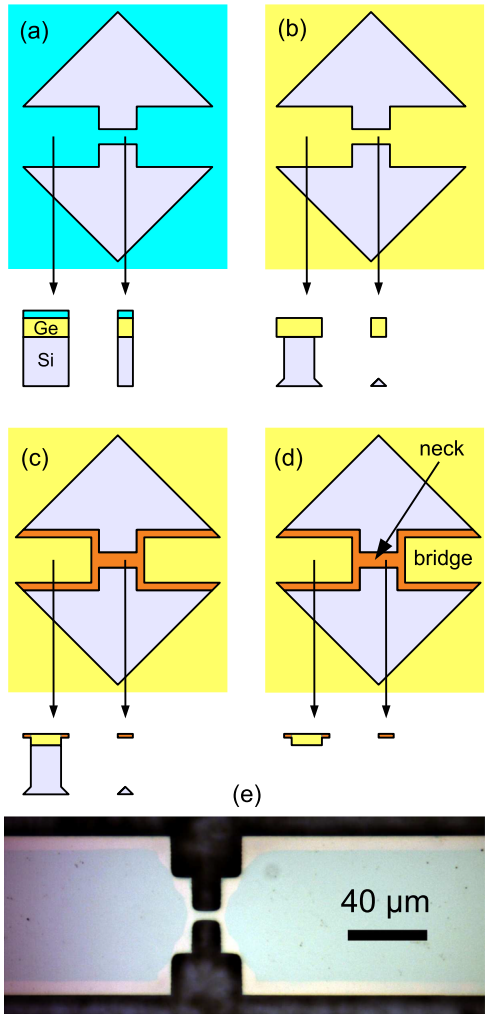

FIG. 2. Top and cross-section schematic view of the fabrication process steps: (a) Bridges and necks patterned by means of optical photolithography and RIE. (b) Selective etching of Si cap layer (light blue) and Si substrate (grey) below the necks. Bridges remain standing on Si pillars. (c) Reduction of neck thickness by selective etching of Ge (yellow) from both top and bottom sides. Thinned Ge regions are colored in orange. (d) Release of bridges by selective etching of Si pillars. (e) Optical microscope picture of bridge and neck. The neck and thinner edges of the bridge have a lighter color than the central region of the bridges due to the difference in thickness.

microscope using a 514 nm (green) laser with 0.3 cm^{-1} spectral resolution. Integration time and laser power were adjusted to produce a good spectral signal-to-noise-ratio and to avoid heating on the thin Ge layer, as discussed above. High resolution Raman maps were collected using the following parameters; 50× objective, 250 nm step size in both the x and y axes. Each map took about 12 hours to complete.

Layer thicknesses of unpatterned regions can be routinely measured by ellipsometry, but the neck area is too small compared to the light spot size available in the ellipsometer used in this study. While tilted SEM images could, in principle, provide a thickness estimation, it relies on finding by chance a broken bridge where the edge is conveniently exposed for observation. The thickness value that can be estimated from these images bears an uncertainty that is too large for such thin Ge layers, being close to our SEM resolution limit. To overcome this difficulty, pump-and-probe reflectivity measurements based on an asynchronous optical sampling technique (ASOPS)[17] were used to obtain reliable measurements of the neck thickness. The frequency of the first order dilatational mode was determined accurately by this method. This frequency is directly related to the thickness of the unsupported layer.

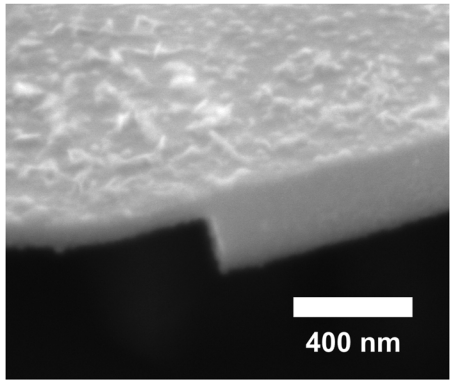

FIG. 3. Cross-section of a broken bridge observed by scanning electron microscopy (SEM). Difference in thickness between the central region (right side in the picture) and the periphery (left side in the picture) of the bridge is clearly observed.

The ASOPS measurements were performed at the center of the neck, as well as at the bridges, for all samples. Pump and probe beams with a center wavelength of 770 nm and 830 nm, respectively, were generated by two fs Ti:sapphire oscillators with a repetition rate of 1 GHz and an actively stabilized frequency offset of 10 kHz. The laser beams were focused by a 50× microscope objective to a spot

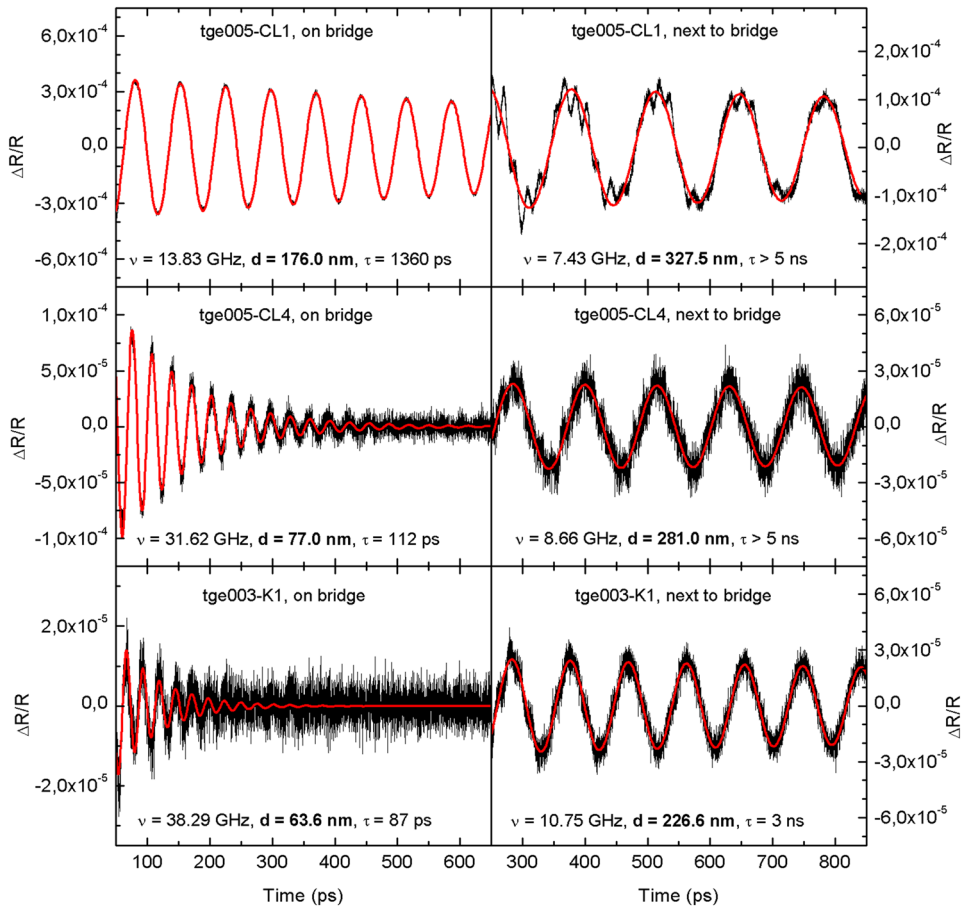

FIG. 4. ASOPS measurements for determination of Ge layer thickness at the bridge and neck. Reflectance oscillations are created by a pump beam with center wavelength of 770 nm. This modulation is detected by a probe beam with center wavelength of 830 nm as a time dependent change in reflectivity arising from the decay of the out of plane acoustic phonons (D_1). Thickness h of the unsupported Ge layer is then determined from the frequency of the D_1 mode.

size of about 1.5 μm and overlapped on the samples in the same spot. The pump beam generates a small thickness modulation of the unsupported Ge layer by the excitation of the dilatational (out of plane) acoustic phonon mode. This modulation is detected by the probe beam as a time dependent change in reflectivity arising from the decay of the out-of-plane acoustic phonons (D_1). The thickness h of the unsupported Ge layer is then determined through the frequency of the D_1 mode, following the relationship $h = \nu_L/2f$, where ν_L = 4870 m/s is the longitudinal sound velocity of Ge and f is the measured frequency of the oscillations.[17] Figure 4 shows reflectivity oscillations measured in the bridge and neck regions of three samples with different neck thickness using the ASOPS technique. The amplitude of the measured signal, i.e. the time dependent change of the reflectivity, depends on the thickness of the suspended material and the wavelength of the probe laser. The reason is, that the thin suspended areas behave like Fabry-Perot cavities in which reflection, absorption, and transmission vary strongly as function of the optical cavity thickness.[22] For a given probe wavelength, the relative intensity of the reflectance due to the pump induced thickness modulation therefore depends on the thickness of the material as was observed e.g. also in the case of suspended Si membranes.[23] The deviation from a pure damped sinusoidal curve in the bridge region of sample 1 (Fig. 4, top right panel) originates from the presence of higher order dilatational modes with non-zero out-of-plane displacement (D_3, D_5, D_7, ...) whose intensity follows an $1/\omega^2$ relationship in the Fourier transform of the time traces.[24]

RESULTS

Table I presents results of three different samples that differed in their geometrical parameters, as a different strain concentration in the neck region occurred. The slight bisotropic tensile strain in the bridges at both sides of the neck will be concentrated in the neck region. When the suspended structure is released from the Si substrate by the etching procedure, both bridges contract to relax the tensile strain. In this way, the neck is uniaxially stressed, leading to an enhancement of its tensile strain by a large factor. We define the enhancement factor (EF) as the ratio between uniaxial strain in the neck and biaxial strain in the Ge layer before processing. Values of the EF obtained from Raman spectra are also listed in Table I for three membranes with different final uniaxial tensile strain. The EF can be also estimated from the geometrical dimensions of bridge and neck using the following equation:

$$EF_{geo} = \frac{1 + \dfrac{A}{B-A}}{\dfrac{h_1}{h_2} \cdot \dfrac{a}{b} + \dfrac{A}{B-A}} \tag{1}$$

where a and A are the width and length of the neck, b and B are the width and length of the bridge, h_1 and h_2 are the thickness of the neck and the bridge, respectively. This equation is derived from Eq. (1) in Ref. 12, taking into consideration that in our samples not only the neck is narrower

TABLE I. Measurements of Ge membranes with uniaxial tensile strain.

Parameter	Method	Sample 1	Sample 2	Sample 3
A (μm)	Opt. Microscope	12.6	12.6	12.2
a (μm)	Opt. Microscope	6.2	6.2	6.2
B (μm)	Opt. Microscope	740	740	340
b (μm)	Opt. Microscope	80	80	70
h epi (μm)	Ellipsometry	458	458	350
h_1 neck (μm)	ASOPS	0.176	0.077	0.064
h_2 bridge (μm)	ASOPS	0.328	0.281	0.227
ϵ_{biax}(%)	Raman Spectroscopy	0.12	0.12	0.10
EF_{geo}	Eq. (1)	17.3	26.6	16.7
ϵ_{uniax}(%)	Raman Spectroscopy	2.0	3.2	1.7
EF	Raman Spectroscopy	16.5	25.8	17.4
Strain (%)	FEM	2.96	3.09	1.51
EF	FEM	16.1	25.3	15.9

than the bridge by a factor a/b, but it is also thinner by a factor h_1/h_2. In this way, uniaxial tensile strain up to high values in excess of 3% can be achieved just by modifying the geometrical design.

The crystalline quality of the samples is of paramount importance to attain the desired optical and electrical properties. Figure 5(a) shows a cross-sectional TEM image of the epitaxial layers (Si/Ge/Si). A high density of dislocations is observed near the interface between the Si substrate and the Ge layer and in the Si cap layer. Few threading dislocations are observed in the Ge away from the interface. Precisely those regions with high dislocation density are eliminated during the thinning of the necks by the selective KOH etching. Figure 5(b) shows a large-area TEM planar view image of the germanium layer thinned down to 100 nm by ion milling. The thinned Ge layer is partially transparent to electrons. Dark lines are the planar projection of threading dislocations. Their number is so low that they can be counted directly, obtaining a threading dislocation density of about 10^7 cm^{-2}. These observations confirm that the etched Ge layer constituting the bridges and the necks has a high crystalline quality.

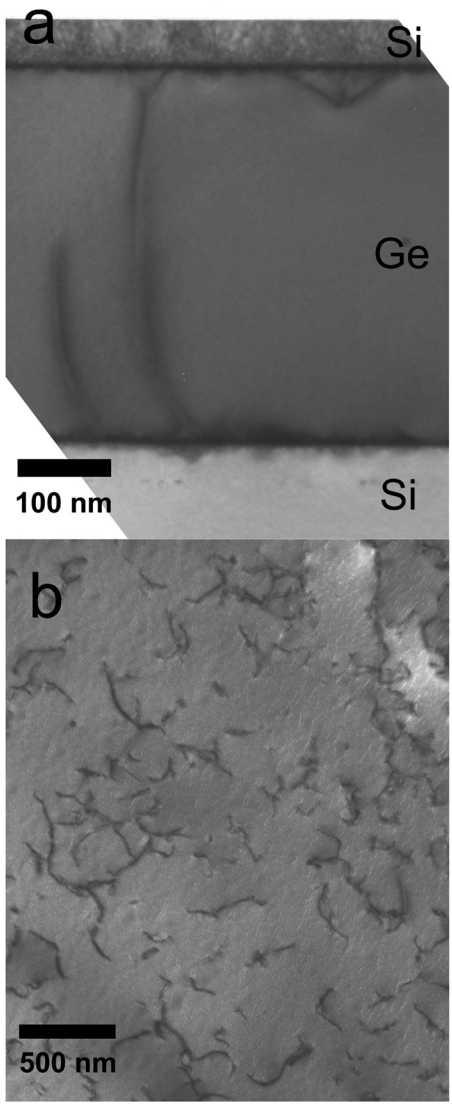

FIG. 5. (a) Cross-section TEM image of the epitaxial layers. From bottom to top, Si substrate, Ge layer and Si cap layer can be observed. (b) TEM image of Ge layer thinned by ion milling from both sides, showing threading dislocations present in the material.

The three-fold degeneracy of the optical phonon modes of Ge at the Brillouin-zone center is lifted due to the tetragonal distortion caused by either the biaxial stress in the unpatterned regions or the resulting uniaxial stress of the suspended parts of the structure. The zone-center phonon split into a singlet (s) and a doublet (d) component. For the case of Raman measurements in backscattering geometry from the (001) surface only the longitudinal optical (LO) mode is allowed by symmetry.[25] It is crucial to note that whereas for the biaxial stress in the x,y-plane the LO mode corresponds to the singlet component, for the uniaxially stressed bridge and neck regions the LO phonon is one of the doublet components. In practice, for the spectroscopic determination of strain one needs to know the so-called strain shift coefficient ($b_{s,d}$), defined as:[26,27]

$$\omega_{s,d} = \omega_0 + b_{s,d} \cdot \Delta\varepsilon \tag{2}$$

Here ω_0 is the unstrained frequency and $\Delta\varepsilon$ is the elastic deformation (strain) leading to the shift of the singlet or doublet with respect to ω_o. The expression of the strain shift coefficient in terms of the phonon deformation potentials is different for singlet and doublet but, more importantly, depends on the stress status being biaxial, uniaxial or hydrostatic.[28–30] For the biaxial stress case (singlet component) and the uniaxial stress case (doublet component) the corresponding strain shift coefficient reads, respectively:

$$b_s = \omega_0 \cdot \left(\tilde{K}_{11} \cdot {}^{\alpha}\!/_{2} + \tilde{K}_{12}\right) \quad with \quad \alpha = \frac{2C_{12}}{C_{11}} \tag{3}$$

$$b_d = -\frac{\omega_0}{2\alpha} \cdot \left(\tilde{K}_{11} + (1-\alpha) \cdot \tilde{K}_{12}\right) \quad with \quad \alpha = \frac{C_{11} + C_{12}}{C_{12}} \tag{4}$$

Using the literature values for pure Ge, namely, ω_0 = 300.8 cm^{-1} for the unstrained LO frequency, C_{11} = 129 GPa and C_{12} = 48.3 GPa for the elastic constants, and K_{11} = −1.66, K_{12} = −2.19 for the LO-phonon deformation potentials,[31] Eqs. (3) and (4) yield b_s = −460(20) cm^{-1} and b_d = −170(10) cm^{-1} for the strain shift coefficients. Figure 6 shows the Raman spectra of a sample with a neck thickness of 76 nm. Raman spectra were measured in three positions: at the neck center, at the center of one bridge, and on a broken bridge. The Ge–Ge mode peak measured in the starting biaxially stressed Ge layer shifts by −0.6 cm^{-1} with respect to the relaxed Ge peak, corresponding to ε_{biax} ~0.12% biaxial tensile strain. The Ge–Ge mode measured in the neck moves by up to −5.3 cm^{-1}

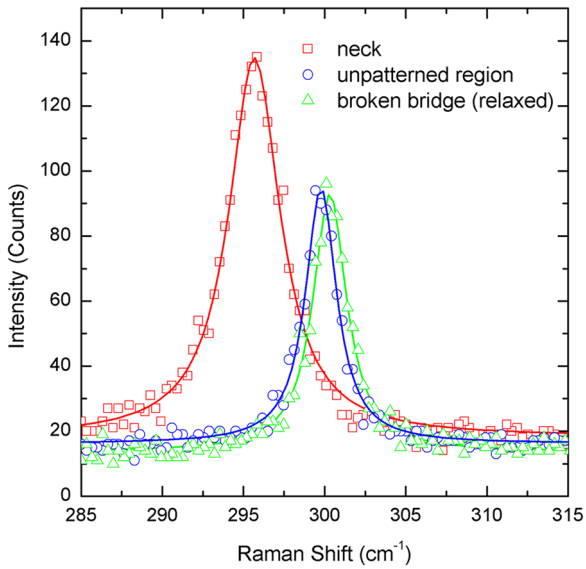

FIG. 6. Raman spectra measured at the neck and unpatterned region on sample 2. A spectrum measured at a broken bridge is included as reference for Ge free of strain (green triangles). Tensile strain in the Ge layer reduces the Raman shift. The biaxial strain in the Ge layer in unpatterned regions produces a slight reduction of Raman shift (blue circles), while the high uniaxial tensile strain in the neck produces a large reduction of Raman shift (red squares).

with respect to the relaxed Ge peak, corresponding to a uniaxial strain ε_{uniax} ~3.1%. Peaks were fitted accurately by a Lorentzian line shape, indicating that strain is rather uniform in the volume excited by the laser spot. Table I shows strain shift values, as calculated from the Raman peak position, and the physical dimensions of three different samples.

Two-dimensional (2D) Raman spectra maps were measured using a step size of 250 nm to determine the global strain status of the Ge membranes. Simulated strain maps of bridge and neck structures were calculated by finite element method (FEM) models using COMSOL Multiphysics software.[32] We employed known elastic constants, phonon deformation potential parameters, patterning dimensions and etching parameters and compared these simulated maps to the strain maps calculated from Raman measurements. Both Raman strain maps and FEM simulation strain maps are shown in Figs. 7(a) and 7(b), respectively, for two samples. Good agreement between experiment and simulation suggests that the values of stress/strain tensors obtained by FEM simulation are reliable. It is worth noting that Raman mapping does not yield information on whether stress is uniaxial or biaxial. Determination of the stress type, uniaxial or biaxial, is a crucial input for the analysis of the Raman results, for choosing which one of Eqs. (3) and (4) ought to be used to evaluate the strain from the frequency shift. This information is extracted from FEM simulations that deliver the full stress and strain tensors in static equilibrium. In our case, it indicates that tensile stress in the neck is mostly uniaxial. Good matching with Raman maps confirm that these FEM simulations are an accurate method to predict strain distribution when designing membranes. The main discrepancy between our simulations and Raman maps is the strain distribution around neck-bridge contact area. Raman maps show strain spreading along the bridge edge farther than the neck width (vertical direction in Fig. 7). FEM simulations show strain spreading away from the neck edge into the bridge (horizontal

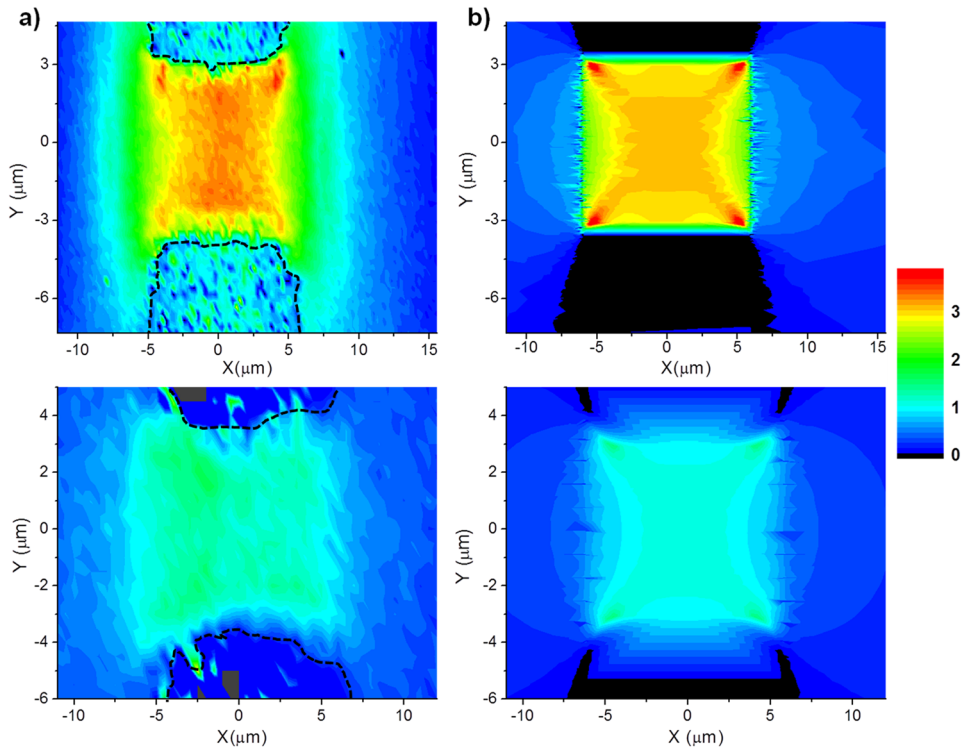

FIG. 7. Two-dimensional maps of the strain distribution in the suspended Ge membranes obtained by Raman spectroscopy and simulations using a finite element method. Raman spectra were collected using a 250 nm step size in the *X* and *Y* axes. Scale of the *X* and *Y* axes is different for a better visualization of the whole neck region (necks are oriented along the *X* direction). (a) Two-dimensional plot of the ε_{11} strain component calculated by applying Eq. (2) to the Raman shift maps measured on sample 2 (top row) and sample 3 (bottom row). Dashed lines are a guide to the eye to show edges of the suspended Ge membrane. (b) Simulated ε_{11} strain maps using finite element method and geometrical dimensions of sample 2 (top row) and sample 3 (bottom row). Color bar represents ε_{11} tensile strain component (%).

direction in Fig. 7). This discrepancy may arise because we did not include in our model the thinner Ge layer along the edge of the bridges that exists in the actual samples. Both Raman maps and FEM simulations also show that strain is rather homogeneous in the neck region, but there is strain accumulation at the corners where the neck is connected to the bridge. Membranes usually break at these corners when trying to obtain a higher strain by modifying geometrical dimensions of bridge and neck. Therefore, these FEM simulations will be useful also to optimize curvature radius at the corners to prevent membrane failure at higher strain.

CONCLUSIONS

Suspended Ge membranes were fabricated with high uniaxial tensile strain from layers deposited by MBE on Si substrates. A fabrication method was established to reduce locally membrane thickness by a two-steps patterning and selective etching process. First, a bridge and neck shape was patterned in the Ge membrane, then the neck was thinned from both top and bottom sides, eliminating Ge near the Si substrate, where most misfit dislocations and point defects are found. This localized reduction of membranes thickness allowed further concentration of strain in the neck region. The challenge of measuring the thickness of a membrane with micrometric size and suspended far away from the substrate was solved by applying an optical characterization method. It has been demonstrated that by adjusting not only the in-plane geometrical shape of neck and bridges, but also adjusting locally their thickness, tensile strain can be further tailored in these structures. In addition, FEM simulations of stress/strain tensor maps allowed us to properly discriminate between places in the structure where stress is biaxial or uniaxial. This is instrumental for the correct interpretation of Raman results since the resulting strain value depends on the particular strain-shift coefficient used.

ACKNOWLEDGMENTS

The authors acknowledge financial support from the Spanish Ministry of Economy and Competitiveness (MINECO) through project Consolider NanoTHERM (Grant No. CSD2010-00044) and program Severo Ochoa (Grants SEV-2013-0295 and SEV-2015-0496), the Spanish projects PHENTOM (FIS 2015-70862P) and HIBRI2 (MAT2015- 70850-P) and the postdoctoral Marie Curie Fellowship (IEF) HeatProNano (Grant 628197). J.G.R. is grateful to the AGAUR (Generalitat de Catalunya) Beatriu de Pinós grand (BP-B 00211). The Renishaw inVia Reflex spectroscopy was funded by an ARC LIEF grant LE0560680 and a NHMRC/USYD Equipment grant.

[1] J. Liu *et al.*, Phys. Rev. B **70**, 155309 (2004).
[2] R. Geiger, T. Zabel, and H. Sigg, Frontiers in Mater. **2**, 52 (2015).
[3] Y. Ishikawa, K. Wada, J. Liu, D. D. Cannon, H.-C. Luan, J. Michel, and L. C. Kimerling, J. Appl. Phys. **98**, 013501 (2005).
[4] G. T. Reed, G. Mashanovich, F. Y. Gardes, and D. J. Thomson, Nature Photon **4**, 518–526 (2010).
[5] J. Michel, J. Liu, and L. C. Kimerling, Nature Photon **4**, 527–534 (2010).
[6] C. G. Van de Walle, Phys. Rev. B **39**, 1871 (1989).
[7] J. F. Liu, X. C. Sun, D. Pan, X. X. Wang, L. C. Kimerling, J. Michel, and T. L. Koch, Opt. Express **15**, 11272 (2007).
[8] P. Vogl, M. M. Rieger, J. A. Majewski, and G. Abstreiter, Phys. Scr. **T49**, 476–482 (1993).
[9] Y. M. Niquet, D. Rideau, C. Tavernier, H. Jaouen, and X. Blase, Phys. Rev. B **79**, 245201 (2009).
[10] A. Gassenq *et al.*, Appl. Phys. Lett. **107**, 191904 (2015).
[11] O. Aldaghri, Z. Ikonic, and R. W. Kelsall, J. Appl. Phys. **111**, 053106 (2012).
[12] R. A. Minamisawa, M. J. Süess, R. Spolenak, J. Faist, C. David, J. Gobrecht, K. K. Bourdelle, and H. Sigg, Nature Commun **3**, 1096 (2012).
[13] M. J. Süess, R. Geiger, R. A. Minamisawa, G. Schiefler, J. Frigerio, D. Chrastina, G. Isella, R. Spolenak, J. Faist, and H. Sigg, Nature Photon **7**, 466 (2013).
[14] Y. Ishikawa, K. Wada, D. D. Cannon, J. Liu, H. Luan, and L. C. Kimerling, Appl. Phys. Lett. **82**, 2044 (2003).
[15] D. Back and J. Lee, J. Nanosci. Nanotechnol. **14**, 8999–9004 (2014).
[16] C. K. Maiti and G. A. Armstrong, *Applications of Silicon-Germanium Heterostructure Devices*, Chapter 2, IOP Pub., Bristol and Philadelphia (2001).
[17] A. Bartels *et al.*, Rev. Sci. Instrum. **78**, 035107 (2007).
[18] A. Gassenq *et al.*, Appl. Phys. Lett. **108**, 241902 (2016).
[19] Y. H. Luo, J. Wan, R. L. Forrest, J. L. Liu, G. Jin, M. S. Goorsky, and K. L. Wang, Appl. Phys. Lett. **78**, 454 (2001).
[20] E. Kasper, K. Lyutovich, M. Bauer, and M. Oehme, Thin Solid Films **336**, 319 (1998).
[21] W. Yeh, A. Matsumoto, K. Sugihara, and H. Hayase, ECS J. Sol. State Sci. Technol. **3**, Q195 (2014).
[22] E. Chávez-Ángel, J. S. Reparaz, J. Gomis-Bresco, M. R. Wagner, J. Cuffe, A. Shchepetov, M. Prunnila, J. Ahopelto, F. Alzina, and C. M. Sotomayor Torres, APL Materials **2**, 012113 (2014).

[23] J. Cuffe, O. Ristow, E. Chávez, A. Shchepetov, P.-O. Chapuis, F. Alzina, M. Hettich, M. Prunnila, J. Ahopelto, T. Dekorsy, and C. M. Sotomayor Torres, Phys. Rev. Lett. **110**, 095503 (2013).
[24] M. R. Wagner, B. Graczykowski, J. S. Reparaz, A. El Sachat, M. Sledzinska, F. Alzina, and C. M. Sotomayor Torres, Nano Letters **16**, 5661 (2016).
[25] E. Anastassakis and M. Cardona, Semicond. Semimet. **55**, 117 (1998).
[26] F. Cerdeira, A. Pinczuk, J. C. Bean, B. Batlogg, and B. A. Wilson, Appl. Phys. Lett. **45**, 1138 (1984).
[27] M. Stoehr, D. Aubel, S. Juillaguet, J. L. Bischoff, L. Kubler, D. Bolmont, F. Hamdani, B. Fraisse, and R. Fourcade, Phys. Rev. B **53**, 6923 (1996).
[28] J. S. Reparaz, A. Bernardi, A. R. Goñi, P. D. Lacharmoise, M. I. Alonso, M. Garriga, J. Novák, and I. Vávra, Appl. Phys. Lett. **91**, 081914 (2007).
[29] J. S. Reparaz, A. R. Goñi, A. Bernardi, M. I. Alonso, and M. Garriga, Phys. Status Solidi B **246**, 548 (2009).
[30] T. Etzelstorfer, A. Wyss, M. J. Süess, F. F. Schlich, R. Geiger, J. Frigerio, and J. Stangl, Meas. Sci. Technol. **28**, 025501 (2017).
[31] J. S. Reparaz, A. Bernardi, A. R. Goñi, M. I. Alonso, and M. Garriga, Appl. Phys. Lett. **92**, 081909 (2008).
[32] COMSOL Multiphysics Reference Manual, version 5.3, COMSOL Inc, www.comsol.com.